

Simulation and 3D Reconstruction of Side-looking Sonar Images

E. Coiras and J. Groen
NATO Undersea Research Centre (NURC)
Italy

1. Introduction

Given the limited range and applicability of visual imaging systems in the underwater environment, sonar has been the preferred solution for the observation of the seabed since its inception in the 1950s (Blondel 2002). The images produced by the most commonly used side-looking sonars (side-scan and, more recently, synthetic aperture sonars) contain information on the backscatter strength recorded at every given range. This backscatter strength mainly depends on the composition and the orientation of the observed surfaces with respect to the sensor.

In this chapter, the relations between surface properties (bathymetry, reflectivity) and the images resulting when the surface is observed by side-looking sonar (backscatter strength) are studied. The characterization of this sonar imaging process can be used in two ways: by applying the forward image formation model, sonar images can be synthesized from a given 3D mesh; conversely, by inverting the image formation model, a 3D mesh can be estimated from a given side-looking sonar image. The chapter is thus divided in two main parts, each discussing these forward and inverse processes. The typical imaging sensor considered here is an active side-looking sonar with a frequency of hundreds of kilohertz, which usually allows for sub-decimetres resolution in range and azimuth.

2. Sonar simulation

Simulation is an important tool in the research and development of signal processing, a key part of a sonar system. A simulation model permits to study sonar performance and robustness, giving the analyst the opportunity to investigate variations in the sonar results as a function of one system parameter, whilst keeping other parameters fixed, hereby enabling sensitivity studies. A sonar simulator can be used as well for image data base generation, as an addition to costly measured data of which there is typically a shortage. A data base with sufficient actuality and variability is crucial for testing and developing signal processing algorithms for sonar image analysis, such as object detectors and classifiers. An example is illustrated in Fig. 1, where a measured synthetic aperture sonar (SAS) image of a cylinder sitting on the seafloor and a simulated image of a similar object at the same range are shown.

Source: *Advances in Sonar Technology*, Book edited by: Sergio Rui Silva,
ISBN 978-3-902613-48-6, pp. 232, February 2009, I-Tech, Vienna, Austria

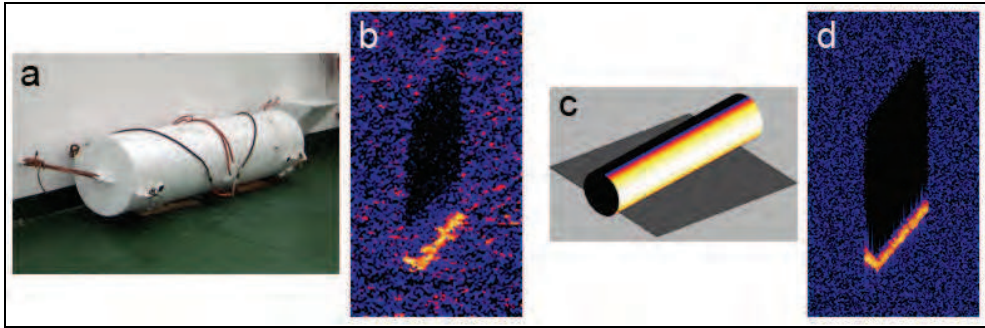


Fig. 1. (a) NURC's test cylinder. (b) Image of the cylinder measured with MUSCLE's synthetic aperture sonar (SAS). (c) 3D computer model of a cylinder and (d) its corresponding sonar image simulated with the SIGMAS model.

2.1 Sonar fundamentals

The basic idea behind any sonar system is as follows: an acoustic signal (or ping) is emitted by the sonar into an area to be observed; the sonar then listens for echoes of the ping that have been produced when bouncing back from the objects that might be present in the area. Typically, sonar images are produced by plotting the intensity measured back by the sonar versus time, and since the speed of sound underwater is known (or can be measured), the time axis effectively corresponds to range from the sonar.

In this way, just as light illuminates a scene so that it can be perceived by an optical sensor, the acoustic ping "ensonifies" the scene so that it can be perceived by an acoustic sensor. Also, as it happens in the optical field, imaging can be approached as a ray-tracing or a wave propagation problem.

2.2 The acoustic wave equation

The propagation of acoustic waves is described by the acoustic version of the wave equation (Drumheller 1998), a second order differential equation for acoustic pressure p , which is a function of time (t) and space (x, y, z). Assuming constant water density and constant sound speed (c) it can be written as:

$$\frac{\partial^2 p}{\partial x^2} + \frac{\partial^2 p}{\partial y^2} + \frac{\partial^2 p}{\partial z^2} - \frac{1}{c^2} \frac{\partial^2 p}{\partial t^2} = -\delta(x - x_s, y - y_s, z - z_s) s(t) \quad (1)$$

The physical process starts with a normalized acoustic wave signal $s(t)$ emitted by a source located at (x_s, y_s, z_s) . In the equation the source is modelled as a point source, with a Dirac delta (δ) spatial distribution function.

When the propagation of sound is described by Eq. 1, the expression for $p(\mathbf{x}; t) = p(x, y, z; t)$ in the case of an infinite water mass around the source is given by:

$$p(\mathbf{x}; t) = \frac{s\left(t - \frac{r}{c}\right)}{4\pi r} \quad (2)$$

Where r is the range from the sonar's acoustic source:

$$r = \sqrt{(x - x_s)^2 + (y - y_s)^2 + (z - z_s)^2} \quad (3)$$

From Eq. 2 it is clear that the acoustic pressure level is reduced according to the reciprocal of the distance to the source. This loss in acoustic pressure and energy is referred to as spherical spreading loss, and in the case of sonars it is to be applied twice: a signal travels from source(s) to target(s) and then back from target(s) to receiver(s). The signal received back at the sonar is a delayed and attenuated version of the initially transmitted signal.

It should be noticed that Eq. 2 is obtained with the assumption that the acoustic source is a monopole and has no dimensions. If this is not the case, p becomes frequency dependent.

2.3 Practical approaches to sonar simulation

From the implementation point of view, several approaches to sonar simulation are possible and frequently hybrid models are implemented. The most common are as follows:

Frequency domain models

In this approach the Fourier transform of the acoustic pressure that is measured back at the sonar receiver is expressed in terms of the Fourier transform of the acoustic pulse used for ensonifying the scene. This is the approach used in NURC's SIGMAS simulator and is discussed in detail in section 2.4. This implementation has the advantage of simplifying the inclusion of several processes that are easier to represent in Fourier space, such as the matched filtering of the received signal or the inclusion of the point spread function (PSF) of the sonar transducers.

Finite difference models

The wave equation given in Eq. 1 can be solved numerically by applying finite difference modelling, which imposes discretizations in time and space dimensions. Using, for instance, a forward difference scheme permits to approximate the time derivative of the pressure as follows:

$$\frac{\partial p}{\partial t} \approx \frac{p(x, y, z; t + \Delta t) - p(x, y, z; t)}{\Delta t} \quad (4)$$

where Δt is the temporal discretization step. For the spatial derivatives (with respect to the x , y , z coordinates) a similar formula is used. Starting the computation with initial conditions, i.e. the acoustic field at $t = 0$, permits to estimate the pressure field as any other point of time and space. The problem with finite difference models when applied to the side-looking sonar case is the dimensions of the computation. In order to obtain an accurate acoustic pressure field the sampling in both space and time is required to be on the order of a fraction of the reciprocal of the frequency and the wavelength, respectively. Even when avoiding parts of the computation—for instance solving only the wave equation around the location of the object of interest—the problem cannot be practically approached for frequencies higher than several kilohertz.

Finite Element (FEM) and Boundary Element models (BEM)

The finite element models and boundary element models are alternatives to finite differences that discretize the problem in a more optimized way. These approaches are complex to implement but typically generate more stable and accurate results with lower computational costs. However, even with these more sophisticated numerical techniques, no reasonable computation times have been achieved for sonar image modelling for frequencies much higher than ten kilohertz.

Ray tracing

Ray tracing (Bell 1997) is a method to calculate the path of acoustic waves through the system of water, sea bottom, sea surface and objects of interest. When the sound speed cannot be assumed constant in the water column refraction of the rays results in bent rays focused to certain places. The paths of the rays are advanced until they hit an object, where the particular contribution of the ray to the returned signal is then computed. Reflection, refraction and scattering events can be accurately modelled by computing a large number of rays, and these can account for complex phenomena observed in sonar imaging, such as multi-path effects or the behaviour of buried targets. Generally speaking, ray tracing is capable of rendering very accurate images but at a high computational cost.

Rasterization

Most current computer graphics are generated using rasterization techniques, which are based on decomposing the scene in simple geometrical primitives (typically triangles) that are rendered independently of each other. This permits fast generation of synthetic images, although effects that require interaction between primitives (such as mirror-like objects) can be complicated to simulate. A big advantage of raster methods is that most current computers include specialized hardware (Graphical Processing Units, or GPUs) that greatly accelerate raster computations. NURC is currently working on a GPU-based implementation of its SIGMAS sonar simulator, in order to achieve faster simulation performance.

2.4 The SIGMAS sonar simulator

Using the frequency domain approach followed by the SIMONA model (Groen 2006) the SIGMAS simulator calculates the acoustic pressure for every pixel in the sonar image at the same time. In this sense, the signal processing, i.e. the imaging algorithm, is included in the model. In order to develop a realistic but sufficiently fast model some assumptions have been made. The sound speed in the water column is assumed to be constant, which means that acoustic paths follow a straight line. The surfaces of simulated objects are assumed discretized into facets to which the Kirchhoff approximation to the scattered field is applied.

The general expression in frequency domain for the acoustic pressure at the receiver \mathbf{x}_r outside of an object's surface A can be derived using Green's theorem (Clay 1977, Karasalo 2005):

$$P(\mathbf{x}_r; f) = \iint_{\mathbf{x} \in A} [G(\mathbf{x}_r, \mathbf{x}; f) \nabla P(\mathbf{x}; f) - P(\mathbf{x}; f) \nabla G(\mathbf{x}_r, \mathbf{x}; f)] \cdot \mathbf{n}(\mathbf{x}) dA \quad (5)$$

In the expression, \mathbf{n} is the surface normal and G is Green's function, which for a homogeneous medium is given by (Neubauer 1958):

$$G(\mathbf{x}_r, \mathbf{x}; f) = \frac{e^{ik|\mathbf{x}-\mathbf{x}_r|}}{4\pi|\mathbf{x}-\mathbf{x}_r|} \quad (6)$$

Where $k = 2\pi f / c$ is the wave number.

On hitting a surface, part of the pressure wave will be scattered back (reflected) and some of it will be refracted into the surface material or absorbed as heat. The fraction of pressure that is returned is measured by the reflectivity (or reflection coefficient) R of the surface material. The surface boundary conditions that relate the incident (P_i) and scattered (P) waves are:

$$P(\mathbf{x}; f) = (1 + R(\mathbf{x}; f)) P_i(\mathbf{x}; f) \quad (7)$$

$$\frac{\partial P(\mathbf{x}; f)}{\partial n} = 1 - R(\mathbf{x}; f) \quad (8)$$

Where n indicates variation in the direction normal to the surface.

For our simulation purposes, an object with an acoustically rigid surface can be assumed, which means the reflectivity R is set to unity and therefore elastic effects do not play a role. This simplifies the boundary conditions on the scattering surfaces and is the approach used by SIGMAS. Substituting R for 1 in the boundary conditions (7) and (8), and using Green's function (6) twice to propagate from source \mathbf{x}_s to surface A and then to receiver \mathbf{x}_r yields the expression:

$$P(\mathbf{x}_r; f) = \iint_{x \in A} -\frac{i e^{i\mathbf{k} \cdot (\mathbf{x}_r - \mathbf{x}_s)} e^{i\mathbf{k} \cdot (\mathbf{x} - \mathbf{x}_s)}}{\lambda |\mathbf{x} - \mathbf{x}_r| |\mathbf{x} - \mathbf{x}_s|} P(\mathbf{x}_s; f) \frac{\mathbf{x} - \mathbf{x}_r}{|\mathbf{x} - \mathbf{x}_r|} \cdot \mathbf{n}(\mathbf{x}) dA \quad (9)$$

Knowing that in sonar the source and the receiver are in the same position—which from now on we assume to be at the coordinate origin—and assuming the surface is discretized on small facets of area a^2 , the integral can finally be expressed as the following summation:

$$P(f) = \frac{a^2}{\lambda} \sum_k \frac{\hat{\mathbf{n}}_k \cdot \hat{\mathbf{r}}_k}{\|\mathbf{r}_k\|^2} S(f) e^{i \frac{2\pi f}{c} \|\mathbf{r}_k\|} \quad (10)$$

Where \mathbf{r}_k is the vector from the sonar to the k^{th} surface element, $S(f)$ is the Fourier transform of the transmit signal $s(t)$, and where the hats indicate unit vectors.

Application of Eq. 10 produces results as those presented in Fig.2, where a barrel sitting on flat sand and a truck wheel on a bumpy clay floor have been simulated.

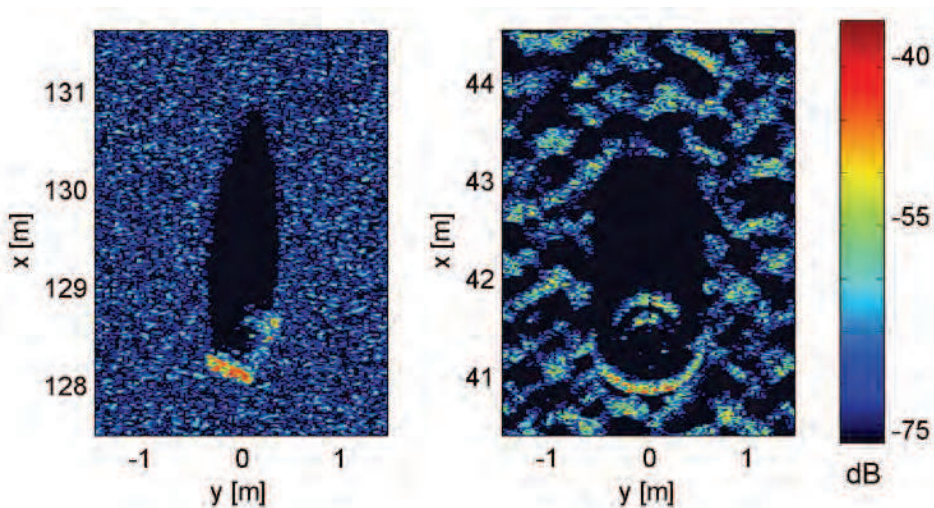


Fig. 2. Two examples of the output produced by the SIGMAS simulator: a barrel sitting on a sandy seafloor at 128 meters distance, and a truck wheel at 41 meters distance on a bumpy clay seabed.

2.5 Model simplification

The approach to simulation used by SIGMAS produces very accurate results that correlate well to experimental data. This accuracy comes with a computational cost, since the coherent model used requires sampling the objects to be simulated at scales smaller than the wavelength of the ensonifying signal. In the examples shown, for instance, the number of discrete point scatterers is around one million per object.

For very smooth objects or if elasticity effects are relevant, coherence has to be considered. On the other hand, if surfaces are rough at wavelength scale, the complex exponentials in Eq. 10 can be dropped and the discretization can use bigger surface elements with an equivalent reflectivity value R . The constructive and destructive interferences described by the complex exponentials can also be replaced by a noise distribution (Bell 1997). Furthermore, since most sonars perform some kind of Time-Varying Gain (TVG) intensity corrections to compensate for the spherical spreading loss, that contribution can also be dropped and replaced by a final image level scaling. Computations can be performed directly in image space, removing also the need for the FFT when working in frequency domain, resulting in the following expression for the observed pixel intensity at surface point \mathbf{r} :

$$I(\mathbf{r}) = K(\mathbf{r}) \sum_k (\hat{\mathbf{n}}_k \cdot \hat{\mathbf{r}}) R_k(\mathbf{r}) \chi_k(\mathbf{r}) \quad (11)$$

Where the sonar is assumed at the coordinate origin, K is a normalization constant that groups all scaling factors and unit conversions, R_k is the reflectivity of the k^{th} surface patch and χ_k is the characteristic function of the patch (one if the circle of radius $|\mathbf{r}|$ intersects the patch, zero if not). Note that Eq. 11 basically corresponds to the Lambertian illumination model for diffuse surfaces (Zhang 1999), where the perceived brightness of a surface point depends on the relative direction of illumination and is independent of the direction of observation.

All these simplifications greatly reduce the complexity of the computations and even permit to use standard computer graphics renderers, such as OpenGL (OpenGL ARB 2004), to create the simulated images. Standard 3D models for objects to be simulated, like the VRML barrel shown in Fig. 3, can also be used directly. The final result is much faster scene

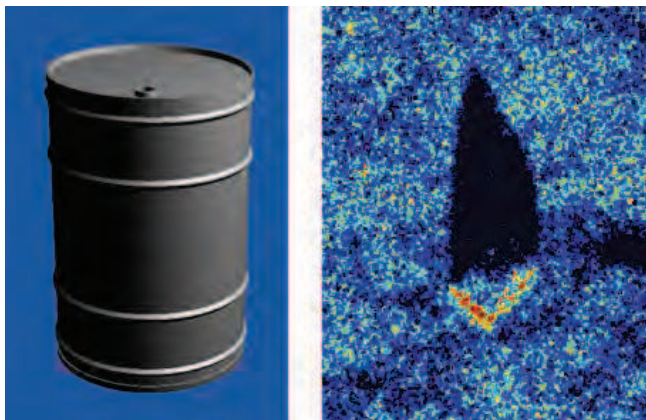


Fig. 3. A three-dimensional VRML model of a barrel and the result of a simplified sonar simulation using standard computer graphics rendering. The barrel is assumed to sit on a rough seafloor at 130 meter distance.

composition and rendering, at the cost of losing the significance of the resulting image values, which are no longer in correspondence with the actual pressure levels.

3. 3D reconstruction of sonar images

This second part of the chapter is dedicated to the sonar inversion process, which allows to infer a computer CAD model from a given sonar image, thus recovering the underlying 3D surface geometry of the observed scene.

3.1 Side-looking sonar image formation model

The geometry of the image formation process for a side-scan sonar is briefly sketched in Fig. 4. The sensor's acoustic source at \mathbf{o} produces an ensonification pulse that illuminates the seafloor. Some of the acoustic energy reaching any seabed point p is scattered back and can be measured by the sensor. The intensity of the corresponding pixel on the side-scan image will be proportional to the amount of energy scattered back from the surface point. The illuminating pulse is not isotropic, but follows a particular beam-profile Φ that depends on the grazing angle a subtended by the vector \mathbf{r} from \mathbf{o} to surface point p .

In the case of synthetic aperture sonar (SAS) the side-looking image is formed differently, by emitting wider acoustic pulses and integrating the returned signals over time (Belletini 2002). For our inversion purposes, however, SAS images can still be regarded as having been produced by a sophisticated side-scan sonar, and the following discussion applies to both types of sensors.

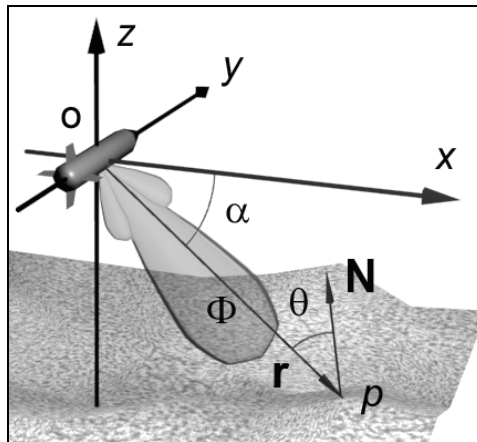


Fig. 4. Side-looking sonar imaging geometry (adapted from (Coiras 2007)).

In order to model the scattering process we use the traditional Lambertian (Zhang 1999) model already described in Eq. 11, which permits one to derive the returned intensity from the parameters defining the observed scene. This simple model for diffuse scattering assumes that the returned intensity depends only on the local angle of incidence θ of the illuminating sound pulse, and not on the direction of observation or on the frequency of the pulse. For the problem to be manageable the surface describing the observed scene has to be univalued, which forces to replace the expression in Eq. 11 for the following simpler one:

$$I(\mathbf{r}) = K \Phi(\mathbf{r}) R(\mathbf{r}) \frac{\mathbf{n} \cdot \mathbf{r}}{\|\mathbf{n}\| \|\mathbf{r}\|} = K \Phi(\mathbf{r}) R(\mathbf{r}) \cos(\theta(\mathbf{r})) \quad (12)$$

Where Φ represents the intensity of the illuminating sound wave at point p , R is the reflectivity of the seafloor, θ is the incidence angle of the wave front and K is a normalization constant. Since most logged side-looking images already include some kind of intensity correction, all the intensity variations caused by the sensor's beam-profile, the spherical spreading loss and the TVG and other corrections are supposed to be grouped under the beam-pattern Φ .

Following (Coiras 2007), with the coordinate system centered at the sensor in \mathbf{o} , the x axis being the across-track ground distance and y pointing along the sensor's trajectory, we have:

$$\begin{aligned} \mathbf{r} &= (x, 0, Z(x, y)) \\ \mathbf{n} &= \left(-\frac{\partial Z}{\partial x}(x, y), -\frac{\partial Z}{\partial y}(x, y), 1 \right) \end{aligned} \quad (13)$$

Where the y coordinate in \mathbf{r} is 0 because the side-scan sonar pulse Φ is shaped so that only the points contained in the x - z plane are illuminated. Note that although this does not directly apply to the sonar pulses used for SAS imaging, the resulting SAS images are to all practical purposes equivalent to a side-scan image with constant resolution in the range direction.

Combination of expressions (12) and (13) yields the forward model for the computation of the intensity I at any point p , given the model parameters R , Z and Φ in ground range coordinates x , y from the sensor:

$$\begin{aligned} I(x, y) &= K \Phi(x, y) R(x, y) \cdot \\ &\frac{Z(x, y) - x \cdot \frac{\partial Z}{\partial x}(x, y)}{\sqrt{x^2 + Z^2(x, y)} \cdot \sqrt{\left(\frac{\partial Z}{\partial x}(x, y)\right)^2 + \left(\frac{\partial Z}{\partial y}(x, y)\right)^2 + 1}} \end{aligned} \quad (14)$$

Where the surface gradients can be approximated by finite differences (as shown for Eq. 4) and where the normalization value K is:

$$K(x, y) = \frac{Z \cdot \sqrt{x^2 + Z^2} \cdot \sqrt{1 + \left(\frac{\partial Z}{\partial y}\right)^2 + \frac{x^2}{Z^2} \left(1 + \left(\frac{\partial Z}{\partial y}\right)^2\right)^2}}{-Z^2 - x^2 \cdot \left(1 + \left(\frac{\partial Z}{\partial y}\right)^2\right)} \quad (15)$$

Where the explicit dependencies on (x, y) have been dropped for clarity.

3.2 Sonar inversion

Equation 14 provides a direct formula for estimating the returned intensity given the model parameters. But the inverse problem—obtaining the model parameters from the observed

intensities—is clearly under-determined, since we only have one observation (of I) at each point to compute the values of the three model parameters.

In order to solve this problem and following (Coiras 2007) we take a least mean squares (LMS) approach to minimize the sum E of the squared differences between the points of the observed image, I , and those rendered by the model in Eq. 14, \hat{I} :

$$E = \sum_{x,y} E(x, y) = \sum_{x,y} (I(x, y) - \hat{I}(x, y))^2 \quad (16)$$

And the following optimization problem needs to be solved:

$$(Z, R, \Phi) = \arg \min (E) \quad (17)$$

A solution can be found by using Expectation-Maximization (EM) (Dempster 1977), which will iteratively converge to an optimal set of modeling parameters. Every iteration of the EM method consists of two stages: in the Expectation stage, the current estimates for the model (R, Φ, Z) are substituted in Eq. 14 to obtain an estimation for the intensity \hat{I} . In the Maximization stage gradient descent is used to locally minimize E , by updating the model parameters as follows:

$$\begin{aligned} R(x, y) &\leftarrow R(x, y) - \lambda \cdot \frac{\partial E}{\partial R}(x, y) \\ \Phi(x, y) &\leftarrow \Phi(x, y) - \lambda \cdot \frac{\partial E}{\partial \Phi}(x, y) \\ Z(x, y) &\leftarrow Z(x, y) - \lambda \cdot \frac{\partial E}{\partial Z}(x, y) \end{aligned} \quad (18)$$

Where λ is a small constant value used to control the rate of change. Direct operation using Eq. 14, 16 and 18 yields:

$$\begin{aligned} R(x, y) &\leftarrow R(x, y) + 2\lambda \cdot \frac{\hat{I}(x, y)}{R(x, y)} (I(x, y) - \hat{I}(x, y)) \\ \Phi(x, y) &\leftarrow \Phi(x, y) + 2\lambda \cdot \frac{\hat{I}(x, y)}{\Phi(x, y)} (I(x, y) - \hat{I}(x, y)) \\ Z &\leftarrow Z - 2\lambda \hat{I} (I - \hat{I}) \cdot \\ &\quad \cdot \left(\frac{-\partial Z / \partial x - \partial Z / \partial y}{1 + (\partial Z / \partial x)^2 + (\partial Z / \partial y)^2} + \frac{1 + x}{x(\partial Z / \partial x) - Z} + \frac{Z}{x^2 + Z^2} \right) \end{aligned} \quad (20)$$

Where the explicit dependence of the parameters on (x, y) has been removed in the last equation for clarity.

The expressions in Eqs. 20 are iterated until the variation in the error E is below a given threshold.

Regularization

As the method is pixel-based, a regularization scheme is needed to smooth the overall solution. A very simple regularization is performed at the end of every iteration by filtering

the estimated reflectivity and beam-pattern maps. Reflectivity values for the points in shadowed areas are set to that of their nearest illuminated neighbors by hexadecagonal dilation (Coiras 1998) of non-shadowed areas. Whereas values of Φ for all the points subtending the same angle α to the sensor are set to their median value, since the beam profile of the sensor is supposed to be constant for each grazing angle α :

$$\Phi(x, y) = \text{Median}\{\Phi(x_0, y_0) \mid \alpha(x_0, y_0) = \alpha(x, y)\} \quad (21)$$

Initialization

The optimization procedure starts by initialization of the R , Z and Φ maps. The reflectivity is set to a constant value (typically 0.9), and the elevation of every point (x, y) is set to that of the first return at $(0, y)$, corresponding to the altitude of the sonar over the seafloor at that point of its trajectory. The initial beam-pattern Φ is set to the original image values I and then regularized using Eq. 21.

Multi-resolution

A multi-resolution implementation of the method described on the paragraphs above results in better convergence and improved results. Implementation of the multi-resolution version starts by the construction of a multi-resolution pyramid by iterated sub-sampling of the source side-looking image. Processing starts at the smallest level (coarser resolution), using the initialization and regularization procedures described in the previous sections. The resulting R , Z and Φ maps from one level are used as initial maps for the next resolution level. The process finishes when the final stage—corresponding to the full resolution image—is processed. Typically 3 levels of multi-resolution are used.

3.3 Sonar inversion results

During the MX3 2005 experiment carried out by NURC and partner nations in La Spezia (Italy), extensive surveys of an area of seabed were performed using several different vehicle and sensor combinations. The Sea Otter autonomous underwater vehicle (AUV), which was equipped with a Klein 2000 side-scan sonar, and one of the seabed images it produced is shown in Fig. 5.

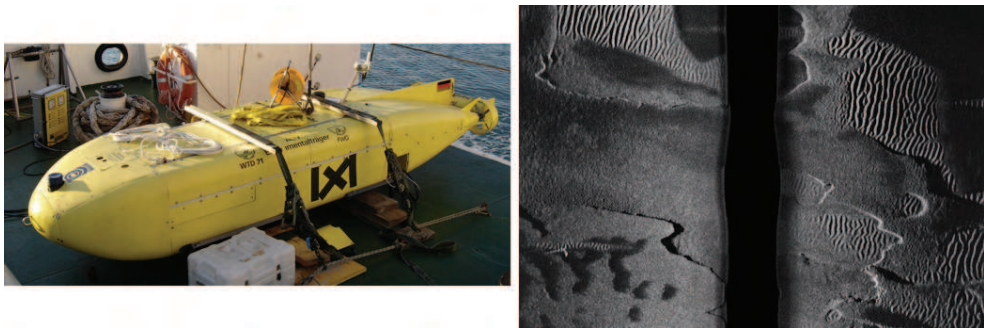


Fig. 5. The Sea Otter AUV and one of the images it collected during the MX3 trials with its Klein 2000 side-scan sonar.

Application of the inversion procedure to the slant-range sonar image of Fig. 5 permits to derive the projection of the sonar's beam-profile, the reflectivity map of the seabed and an estimation of the seabed topography. The maps for these three components are shown in Fig. 6.

The recovered reflectivity, beam-pattern and elevation maps are frequently noisy, which is due to the ill-posed nature of the reconstruction problem; most intensity variations can be caused by changes of any of the three forward model components (Φ , R , Z). Nevertheless, the reflectivity map in Fig. 6 suggests the presence of two different materials in the seafloor: one brighter, responsible for the rippled areas, and a less reflective one on the darker smooth areas. The reconstructed elevation map also looks satisfactory, although its accuracy is difficult to evaluate without actual measures of the area's bathymetry. Additional views of the interesting complex region at the top of Fig. 6(c) are shown in Fig. 7.



Fig. 6. Results of the 3D reconstruction procedure applied to the sonar image shown in Fig. 5. (a) Reflectivity map, (b) projection of the sonar's beam-profile, (c) textured 3D surface reconstruction using the recovered elevation map.

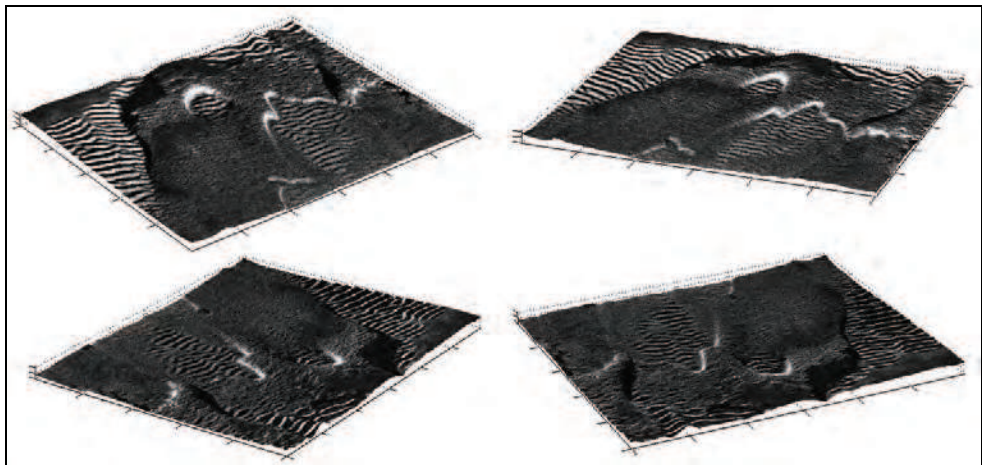


Fig. 7. Zoomed view of a selected area of the reconstructed seafloor, using four different points of view.

Apart from the most visual output of the sonar inversion procedure – the textured elevation map – the different recovered components can also be used for other purposes. As discussed, the reflectivity map hints at the material composition of the seabed. The recovered elevation map can also be used to produce more accurate ground-range projections of side-looking sonar images, one of whose coordinates is originally slant-range; this is relevant when sonar images are to be tiled to produce seamless seafloor mosaics. The recovered beam-profile – which we assume includes as well the intensity corrections (TVG) made during the image formation – has a special interest, in the sense that it is unique for each particular sonar. This means that after processing several sonar files, an estimate of the sensor's beam-profile can be computed and stored for later reference, reducing future inversion problems to the determination of two functions (the reflectivity and the elevation) instead of three.

The projection of the beam-profile is also useful to produce ground-range images with even intensity. As we mentioned already (section 2.2) the spherical spreading loss is responsible for a decrease of signal intensity with range, which is in principle compensated for by a TVG function. Yet there is an additional source of intensity reduction: since points that are far from the sonar subtend lower grazing angles – and therefore lower incidence angles – the average intensity (governed by Eq. 12) further decreases with range. The average incidence angle at a ground range x is:

$$\langle I \rangle(\mathbf{r}) \propto \cos(\langle \theta \rangle(\mathbf{r})) = \langle \hat{\mathbf{n}} \rangle \cdot \frac{\mathbf{r}}{\|\mathbf{r}\|} = (0, 0, 1) \cdot \frac{(x, 0, z)}{\|(x, 0, z)\|} = \frac{z}{\sqrt{x^2 + z^2}} \quad (22)$$

Where the angular brackets indicate expected value, and where the expected value of the unitary surface normal is assumed vertical because the seafloor is mostly flat. Setting the beam-profile to the inverse of Eq. 22 produces the result shown in Fig. 8(c), which features even illumination at all average incidence angles.



Fig. 8. The recovered beam-profile projection can be used to level the intensities of the ground-range version of the sonar image. (a) The original TVG-corrected sonar image in ground-range coordinates after proper projection using the recovered elevation map. (b) How would the image look if the beam-profile of the sonar was isotropic (had the same intensity on all grazing angles). (c) Ground-range image with a modified beam-profile that ensures an even illumination at all average incidence angles; this is the texture map that has been used on Figures 6(c) and 7.

4. Conclusions

The image formation process for side-looking sonar has been studied in this chapter. Both the forward and inverse realizations have been considered, and their application to simulation and 3D reconstruction of sonar images has been shown.

5. Acknowledgements

The authors would like to acknowledge the work of E. Bovio of NURC as scientist in charge of the MX3 experiments, where the Sea Otter vehicle was operated by Atlas Elektronik.

6. References

- J.M. Bell, L.M. Linnett (1997). Simulation and analysis of synthetic sidescan sonar images. *IEE Proceedings on Radar, Sonar and Navigation*, Vol. 144, No. 4, pp. 219–226.
- A. Bellettini, M.A. Pinto (2002). Theoretical accuracy of synthetic aperture sonar micronavigation using a displaced phase-center antenna. *IEEE Journal of Oceanic Engineering*, Vol. 27, No. 4, pp. 780–789.
- P. Blondel and B. J. Murton, (1997). *Handbook of Seafloor Sonar Imagery*. Wiley, New York.
- C. Clay, H. Medwin (1977). *Acoustical Oceanography : Principles and Applications*. John Wiley & Sons Inc.
- E. Coiras, J. Santamaria, C. Miravet (1998). Hexadecagonal Region Growing. *Pattern Recognition Letters*, Vol. 19, pp. 1111–1117.
- E. Coiras, Y. Petillot, D.M. Lane (2007). Multi-Resolution 3D Reconstruction from Side-Scan Sonar Images. *IEEE Transactions on Image Processing*, Vol. 16, No. 2, pp. 382–390.
- A.P. Dempster, N.M. Laird, D.B. Rubin (1977). Maximum Likelihood from incomplete data via the EM algorithm. *Journal of the Royal Statistical Society B*, Vol. 39, No. 1, pp. 1–38.
- D.S. Drumheller (1998). *Introduction to Wave Propagation in Nonlinear Fluids and Solids*. Cambridge University Press, UK.
- J. Groen (2006). *Adaptive Motion Compensation in Sonar Array Processing*. Netherlands Organization for Applied Scientific Research (TNO), The Netherlands.
- I. Karasalo, P. Skogqvist (2005). Identification of Object Parameters from Transient Bistatic Scattering Data. *Proceedings of the Boundary Influences in High Frequency Shallow Water Acoustics Conference*, pp. 357–365. Bath, UK.
- W.G. Neubauer (1958). *Acoustic Reflection from Surfaces and Shapes*. Naval Research Laboratory.
- OpenGL Architecture Review Board (2004). *OpenGL Reference Manual (4th Edition)*, Dave Shreiner. Addison-Wesley Professional.

- R. Zhang, P. Tsai, J. Cryer, M. Shah (1999). Shape from Shading: A Survey. *IEEE Transactions on Pattern Analysis and Machine Intelligence*, Vol. 21, No. 8, pp. 690-706.



Advances in Sonar Technology

Edited by Sergio Rui Silva

ISBN 978-3-902613-48-6

Hard cover, 450 pages

Publisher I-Tech Education and Publishing

Published online 01, February, 2009

Published in print edition February, 2009

The demand to explore the largest and also one of the richest parts of our planet, the advances in signal processing promoted by an exponential growth in computation power and a thorough study of sound propagation in the underwater realm, have lead to remarkable advances in sonar technology in the last years. The work on hand is a sum of knowledge of several authors who contributed in various aspects of sonar technology. This book intends to give a broad overview of the advances in sonar technology of the last years that resulted from the research effort of the authors in both sonar systems and their applications. It is intended for scientist and engineers from a variety of backgrounds and even those that never had contact with sonar technology before will find an easy introduction with the topics and principles exposed here.

How to reference

In order to correctly reference this scholarly work, feel free to copy and paste the following:

E. Coiras and J. Groen (2009). Simulation and 3D Reconstruction of Side-Looking Sonar Images, Advances in Sonar Technology, Sergio Rui Silva (Ed.), ISBN: 978-3-902613-48-6, InTech, Available from: http://www.intechopen.com/books/advances_in_sonar_technology/simulation_and_3d_reconstruction_of_side-looking_sonar_images

INTECH
open science | open minds

InTech Europe

University Campus STeP Ri
Slavka Krautzeka 83/A
51000 Rijeka, Croatia
Phone: +385 (51) 770 447
Fax: +385 (51) 686 166
www.intechopen.com

InTech China

Unit 405, Office Block, Hotel Equatorial Shanghai
No.65, Yan An Road (West), Shanghai, 200040, China
中国上海市延安西路65号上海国际贵都大饭店办公楼405单元
Phone: +86-21-62489820
Fax: +86-21-62489821

© 2009 The Author(s). Licensee IntechOpen. This chapter is distributed under the terms of the [Creative Commons Attribution-NonCommercial-ShareAlike-3.0 License](#), which permits use, distribution and reproduction for non-commercial purposes, provided the original is properly cited and derivative works building on this content are distributed under the same license.